



This open access document is posted as a preprint in the Beilstein Archives at <https://doi.org/10.3762/bxiv.2021.46.v1> and is considered to be an early communication for feedback before peer review. Before citing this document, please check if a final, peer-reviewed version has been published.

This document is not formatted, has not undergone copyediting or typesetting, and may contain errors, unsubstantiated scientific claims or preliminary data.

Preprint Title Revealing the formation mechanism and band gap tuning of Sb₂S₃ nanoparticles

Authors Maximilian Joschko, Franck Yvan Fotue Wafo, Christina Malsi, Danilo Kisić, Ivana Validžić and Christina Graf

Publication Date 15 Juni 2021

Article Type Full Research Paper

Supporting Information File 1 Supporting_Information_Formation mechanism band gap tuning Sb₂S₃ NP Joschko_2021.pdf; 389.8 KB

ORCID® iDs Maximilian Joschko - <https://orcid.org/0000-0002-8462-8019>; Franck Yvan Fotue Wafo - <https://orcid.org/0000-0002-3150-6560>; Danilo Kisić - <https://orcid.org/0000-0001-5541-7020>; Ivana Validžić - <https://orcid.org/0000-0001-9874-8583>; Christina Graf - <https://orcid.org/0000-0002-3308-5640>

License and Terms: This document is copyright 2021 the Author(s); licensee Beilstein-Institut.

This is an open access work under the terms of the Creative Commons Attribution License (<https://creativecommons.org/licenses/by/4.0>). Please note that the reuse, redistribution and reproduction in particular requires that the author(s) and source are credited and that individual graphics may be subject to special legal provisions.

The license is subject to the Beilstein Archives terms and conditions: <https://www.beilstein-archives.org/xiv/terms>.

The definitive version of this work can be found at <https://doi.org/10.3762/bxiv.2021.46.v1>

Revealing the formation mechanism and band gap tuning of Sb_2S_3 nanoparticles

Maximilian Joschko¹, Franck Yvan Fotue Wafo¹, Christina Malsi¹, Danilo Kisić², Ivana Validžić^{2*}, and Christina Graf^{1*}

Address: ¹Hochschule Darmstadt - University of Applied Sciences, Fachbereich Chemie- und Biotechnologie, Stephanstr. 7, D-64295 Darmstadt, Germany

²Vinča Institute of Nuclear Sciences, National Institute of the Republic of Serbia, University of Belgrade, Mike Petrovića Alasa 12-14, 11351 P.O. Box 522, Belgrade, Serbia

Email: Prof. Dr. Ivana Validžić - validzic@vin.bg.ac.rs, Prof. Dr. Christina Graf - christina.graf@h-da.de

* Corresponding authors

Abstract

Sb_2S_3 is a promising nanomaterial for application in solar cells and other fields of electronics and optoelectronics. Sb_2S_3 nanoparticles were prepared via the hot-injection approach. In contrast to earlier work, the reaction temperature was decreased to 150°C, so that the reaction was slowed down and could be stopped at defined reaction stages. Thereby, the formation mechanism of the nanomaterial and the associated kinetics could be revealed. Based on morphological and structural analysis, it is suggested that seed particles (type 0) form immediately after injecting the antimony precursor into the sulfur precursor. These seeds fuse to form amorphous nanoparticles

(type I) that contain a lower percentage of sulfur than that corresponding to the expected stoichiometric ratio of Sb_2S_3 . The reason for this possibly lies in the formation of an oxygen- or carbon-containing intermediate during the seeding process. Afterward, the type I nanoparticles aggregate into larger amorphous nanoparticles (type II) in a second hierarchical assembly process and form superordinated structures (type III). This process is followed by the crystallization of these particles and a layer-like growth of the crystalline particles by an Ostwald ripening process at the expense of the amorphous particles. It was demonstrated that the kinetic control of the reaction allows tuning of the optical bandgap of the amorphous nanoparticles in the range of 2.2 – 2.0 eV. On the contrary, the optical bandgap of the crystalline particles decreases to a value of 1.7 eV and remains constant when the reaction progresses. Based on the proposed formation mechanism, future syntheses for Sb_2S_3 particles can be developed, allowing tuning the particles' properties in a broad range. In this way, the selective use of this material in a wide range of applications will become possible.

Keywords

Sb_2S_3 ; nanoparticles; band gap; solar cells; kinetics

Introduction

The search for efficient, renewable energies with broad availability has become one of the most important challenges of our century. With an usable radiation energy per year several times larger than the world's energy consumption [1], solar energy is a suitable source for future energy supply. However, there are several requirements for materials to be eligible for application in the field of photovoltaics, such as high absorption performance, non-toxicity, abundance, efficiency and low cost.

As a semiconductor with a low bandgap and a high absorption coefficient, antimony(III) sulfide (Sb_2S_3) has become a promising absorption material for photovoltaic applications [2–4]. Furthermore, the material is also suitable for various electronic and optoelectronic applications, such as energy storage [5] or optical data storage [6]. Sb_2S_3 appears in two modifications: an orange, amorphous one and a grayish-black, crystalline one, known as the mineral stibnite [7, 8].

Sb_2S_3 nanomaterials with different morphologies and a broad distribution of band gap values were synthesized by the solvothermal [9], hydrothermal [10], and sonochemical [11] approach, as well as by chemical bath [12], and chemical vapor deposition [13] method. Up to now, the syntheses of Sb_2S_3 nanomaterials lack sufficient control of the growth conditions. The result is nanoparticles whose size, shape and crystallinity can only be tuned to a limited extent. However, for several applications, like electronic circuits [14], or for transferring the synthesis into a microreactor for continuous production [15], it is crucial to adjust these parameters. Mainly two synthesis strategies to gain nanoparticles with uniform size and shape have been described in the literature in the past two decades: the heat-up and the hot-injection method [16]. While the former is rarely applied to synthesize Sb_2S_3 nanoparticles [9], the hot-injection approach has been used in several studies [17–19].

Syntheses reported so far, using the hot-injection method at temperatures between 180 and 240°C [20, 18, 17], yield nanoparticles not smaller than 100 nm or almost instantaneously rods, tubes, or wires in micron size.

Abulikemu et al. investigated the influence of different sulfur and antimony precursors, injection (140 – 220°C) and reaction (100 – 220°C) temperatures, and the overall reaction times (90 s – 2.5 h) on the structural, optical, and morphological properties of Sb_2S_3 nanoparticles via the hot-injection route [19]. They showed that higher injection temperatures lead to smaller nuclei and higher reaction temperatures lead to larger

particles. Furthermore, they concluded that a chlorine-containing antimony precursor affects the morphology and crystallinity of the particles. Nevertheless, the study of Abulikemu et al. focuses on using bis(trimethylsilyl) sulfide (TMS) as sulfur precursor since with this compound, the highest reactivity was reached. However, TMS is toxic and also costly compared to the widely used elemental sulfur, limiting its broad use in the preparation of Sb_2S_3 materials [19].

Li et al. performed mechanistic studies on the temperature dependency of Sb_2S_3 nanoparticles in the range of 180 – 210°C to facilitate the synthesis process following the hot-injection method with a sulfur-oleylamine (S-OIAM) precursor. They found that the temperature influences the crystallinity, shape, and size of the particles [21].

These studies revealed growth processes comprising a primary formation of amorphous Sb_2S_3 nanoparticles, which started to crystallize in an orthorhombic structure and continued to grow. However, in the studies performed so far, both the formation of the nanoparticles and their subsequent growth occurred rapidly. Detailed knowledge of the exact formation and growth mechanisms and, in particular, the associated kinetics of Sb_2S_3 nanoparticles is therefore still lacking. Nevertheless, it is necessary to understand the nanomaterial formation mechanism to achieve control over the morphological and optical properties of the particles, which is crucial for their further application.

In the present work, a hot-injection approach at a moderate temperature (150°C) is presented. The reaction was analyzed in the time sections from 30 s to 30 h. A sulfur-oleylamine precursor was selected to achieve a high reactivity while avoiding toxic substances such as TMS. A relatively low injection temperature was chosen to slow down the reaction rate and, hence, increase the duration of different reaction steps and decrease the primary particle size. Systematically, the Sb_2S_3 nanoparticles in the different formation steps were analyzed regarding their morphology, crystallinity, and

optical properties, and a detailed formation mechanism was proposed. The mechanism involves a seeding process, growth of amorphous particles, crystallization of the particles, and a following growth of the crystals. The synthesis demonstrates that it is possible to tune the band gap of the Sb_2S_3 nanoparticles until the particles reach a fully crystalline state.

Results and Discussion

The Sb_2S_3 nanoparticles were synthesized via a hot-injection synthesis at 150°C , where a complex consisting of Sb and 2-ethylhexanoic acid (Sb-EHA) was injected into a sulfur-oleylamine (S-OIAm) precursor solution. Subsequently, the reaction took place, whose course is characterized by several color changes. Immediately after injecting the precursor, the clear, yellowish reaction mixture turned orange and then red but still stayed clear. After 2 min reaction time, the solution became turbid and changed back to an orange color. Next, the mixture turned red (~20 min) and brown (~8 h) until it finally became greyish-black (~18 h). To follow the formation kinetics of the nanoparticles, the reaction was stopped at different characteristic times by abrupt cooling. Afterward, the received products were washed by repeated centrifugation and redispersion and washing with a 2:3 volumetric mixture of chlorobenzene and 1,2-dichlorobenzene (HAS) to remove excess sulfur [22]. The experiments were repeated at least three times to ensure reproducibility.

Morphology and Structure

At first, the as-synthesized products obtained after different reaction times were characterized by transmission electron microscopy (TEM) (Fig. 1 a-c) and scanning electron microscopy (SEM) (Fig. 1 d-f). The images show that small nanoparticles (type

l) are formed about 2 min (a) after injecting the antimony precursor Sb-EHA. The bright orange product contains nanoparticles of a diameter of 33 ± 5 nm. The nanoparticles are irregularly formed but, in general, spherically shaped.

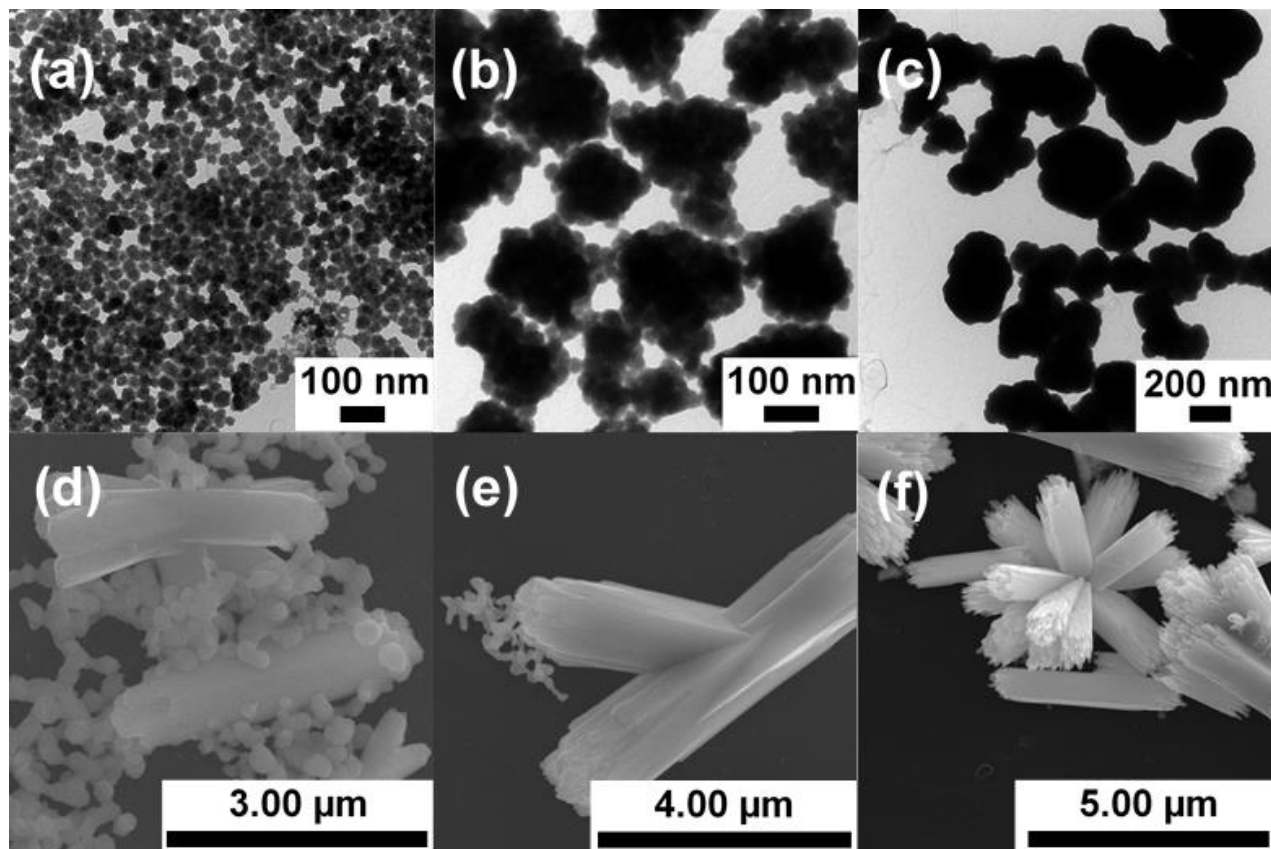


Figure 1: EM images of Sb₂S₃ nanoparticles after different reaction times: (a) TEM, 2 min; (b) TEM, 5 min; (c) TEM, 30 min; (d) SEM, 12 h; (e) SEM, 16 h; (f) SEM, 30 h.

With increasing reaction time, the dispersion turns darker and becomes more reddish. After 5 min (b), larger clusters (type II) were found, consisting of approximately 20-30 smaller individual nanoparticles. The smaller nanoparticles have the same diameter as the type I nanoparticles leading to the assumption that the former ones were aggregating. These aggregates tend to have a spherical shape but are somewhat irregularly formed. Their mean diameter is 210 ± 30 nm. Neither the appearance nor the size (220 ± 30 nm) of the obtained nanostructures significantly changed when stopping the reaction after 10 min (s. Fig. S1 (a) in the Supporting Information).

As the reaction continues, a dark red dispersion is received. While the average particle size remains unchanged (210 ± 30 nm) 30 min after the reaction was started (c), the aggregated type I nanoparticles now appear to have merged as the type II nanoparticles preserved their shape, but no individual type I nanoparticles could be identified in TEM at this stage anymore. Also, the type II nanoparticles appear to have formed superordinated structures (type III). Such multistep hierarchical growth mechanisms were already observed for different materials such as TiO_2 [23], ZnO [24], and Co [25]. For ZnO, Bamiduro et al. also found a merging process after stacks of several nanoplatelets had formed [24].

After 12 h, the dispersion got a brownish color and the first rod-, branch-, and urchin-like particles are found (d). These particles are 2.6 ± 0.9 μm in length with an aspect ratio between 4 and 5 and resemble the type III structures. Still, there are mainly particles of the prior stage remaining.

The crystalline rods grow apparently at the expense of the spherical, amorphous nanoparticles (see XRD below) in an Ostwald ripening process. This assumption is supported by the decreasing diameter of these nanoparticles from 220 ± 30 nm to 150 ± 40 nm, which one can see in Fig. 2, as the reaction progresses from 12 h to 16 h (e) and their decreasing amount (s. Fig. S2 in the Supporting Information). At this stage, the rods have a length of 5.7 ± 1.8 μm . Rod-like crystal growth by the dissolution of spherical, amorphous nanoparticles was already suggested by Validžić et al. for similar processes at a higher temperature [20], supporting this assumption.

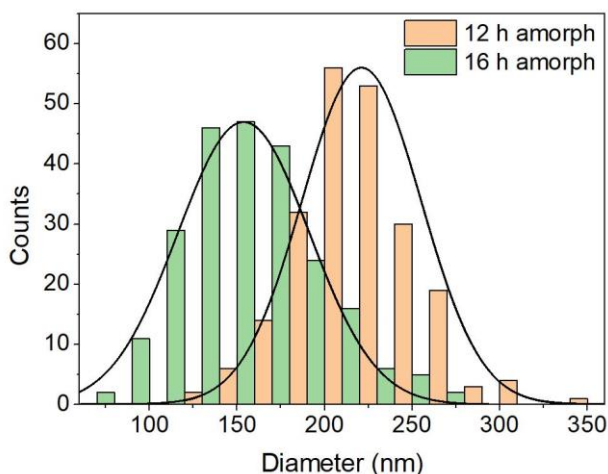


Figure 2: Histograms showing the size distribution of the spherical, amorphous particles in the samples obtained after 12 and 16 h, respectively. A decreasing diameter with progressing reaction time is visible and likely due to Ostwald ripening. The size distribution curves were calculated assuming a Gaussian distribution.

The rods grow anisotropically, i.e., preferentially in the longitudinal direction, as shown by the changing aspect ratio from ~ 4 - 5 to ~ 6 after 12 h and 16 h, respectively. This observation agrees with the findings of authors who describe a growth along the c-axis of Sb_2S_3 nanomaterial [26, 27]. This anisotropic growth corresponds to the orthorhombic structure of stibnite, the crystalline modification of Sb_2S_3 [28].

After 18 h (s. Fig. S1 (b) in the Supporting Information), the solution got grayish-black and no more spherical particles were found. The size of the rods obtained after 18 h is identical compared to that in the sample after 30 h within the measurement uncertainties ($5.5 \pm 1.9 \mu\text{m}$ and $5.4 \pm 1.6 \mu\text{m}$). Histograms of the length and width distribution of the crystalline particles obtained after 16, 18, and 30 h can be found in Fig. S3 in the Supporting Information.

TEM images of growing rods show layered structures (s. Fig. S4 in the Supporting Information) with bristle-shaped tips, which get more distinct with increasing reaction time (s. Fig. S5 Supporting Information). The bristles become thicker but do not appear

to change in length at reaction times between 16 to 30 h. These findings suggest a fiber-like growth at the tips and a layered growth around the individual bristles and the whole rod. However, the particles do not seem to be bundles of nanowires, leading to the assumption that the different, fiber-like growing parts of one particle are fusing. Since the tips remain their bristle-like shape, even after the growth stops after 18 h reaction time, a merging process is excluded. The growth of individual particle fragments, such as the bristles, was described in the literature as a dendrite-like splitting or branching of primary particles in an autoclave synthesis with ethylene glycol or polyethylene glycol as solvent [29, 30]. The authors reasoned the cleavage at the particle tips by weak van-der-Waals forces between $(\text{Sb}_4\text{S}_6)_n$ chains, of which the particles consist, or by strongly bound ligands interfering with the crystal growth, respectively. However, as crystal growth is a kinetically controlled process, mild reaction conditions lead to delayed growth in the preferred direction, and the other crystal planes also grow. Hence, it is likely that integration of the dissolving amorphous particles will fuse the fibers of the crystalline ones. This behavior was also found by Validžić et al. in a different approach of synthesizing Sb_2S_3 nanoparticles at a higher temperature (240°C) [31].

Table 1 gives an overview of the characteristics of the particles received after different reaction times. One can see the size of the amorphous nanoparticles/aggregates, the size and aspect ratios of the crystalline particles, as well as the corresponding molar ratios of Sb and S obtained by EDX, and the associated band gaps obtained by reflectance measurements (s. discussion of the optical data below).

Table 1: Time-dependent characteristics of Sb₂S₃.

Reaction time	Size amorphous particle/aggregate (nm)	Crystalline particles' length (μm)	Crystalline particles' width (μm)	Molar ratio Sb:S (EDX)	Bandgap ±0.03 (eV)
2 min	33±5	-	-	48:52	2.18
5 min	210±30	-	-	41:59	2.12
10 min	220±30	-	-	41:59	2.07
30 min	210±30	-	-	38:62	2.07
12 h	220±30	2.6±0.9	0.6±0.2	41:59	2.01/1.68 ^a
16 h	150±40	5.7±1.8	1.0±0.3	40:60	-/1.72 ^b
18 h	-	5.5±1.9	1.0±0.4	40:60	1.72
30 h	-	5.4±1.6	1.0±0.3	39:61	1.71

^aThe two band gaps correspond to an amorphous and a crystalline species present in the sample (s. main text for details).

^bThe amorphous fraction in this stage is too small to cause a visible slope in the reflectance spectrum.

X-ray powder diffraction (XRPD) measurements of an orange-red (30 min) and a grayish-black (18 h) sample were exemplarily performed to examine the samples' structures. The diffractograms shown in Fig. 3 reveal a low crystallinity for the sample obtained after 30 min (Fig. 3 (a)) as no specific diffraction peaks are found, and a high crystallinity in accordance with the stibnite structure (COD 9003460) for the sample obtained after 18h (Fig. 3 (b)). These results show that the rather spherically shaped orange nanoparticles are mainly amorphous and crystallize into rod-like, grayish-black particles.

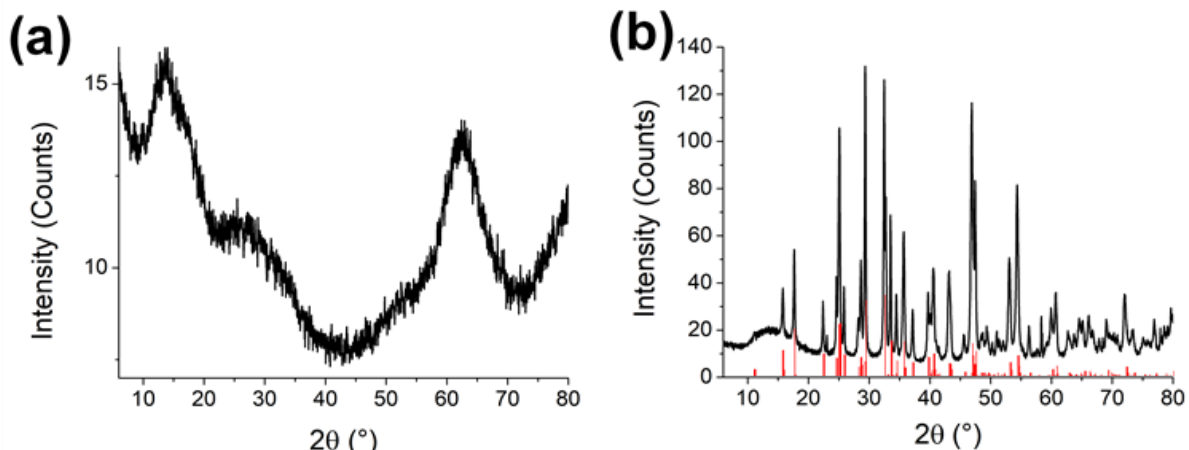


Figure 3: X-ray diffractograms of a sample after a reaction time of (a) 30 min and (b) 18 h (red lines are corresponding to stibnite, COD 9003460).

Thus, the kinetics of the reaction progress can be followed by the dispersion color. As long as there are only amorphous structures present, the dispersion has an orange-red appearance. We assume that some of the amorphous, orange-red type III structures act as crystallization nuclei after 7-9 h. The particles start to crystallize in the shape of the superordinated type III structures described previously, leading to a brownish color. Owing to the preferred growth direction, rods, branch-like, or urchin-like stibnite particles are finally received, which have a grayish-black appearance.

A major advantage of slowing down the reaction kinetics is the possibility of looking at the early stage of the reaction. Therefore, in addition to the experiments described above, the reaction was also stopped after 30 s when the solution was still transparent. In this case, next to nanoparticles of a similar size and shape as the type I nanoparticles obtained after 2 min, an even smaller species of seed particles (type 0) could be observed (Fig. 4 (a)). These type 0 seed particles are 5-10 nm in size and seem to assemble into the larger type I nanoparticles as the latter ones have a raspberry-like appearance (Fig. 4 (a) and (b)). The larger nanoparticles have sizes between 15 and

35 nm (Fig. 4 (b)), with the particle fraction of a size around 35 nm found more frequently (Fig. 4 (c)). Together with the finding that the type I nanoparticles are also around 35 nm in diameter (s. Fig. 1), this leads to the assumption that there is an aggregation and merging step from the type 0 to the type I nanoparticles additional to the one occurring from the type I to the type II nanoparticles. Thus, there is a double hierarchical assembly and subsequent merging process of the amorphous nanoparticles.

It was not possible to isolate visible nanoparticles immediately after injection.

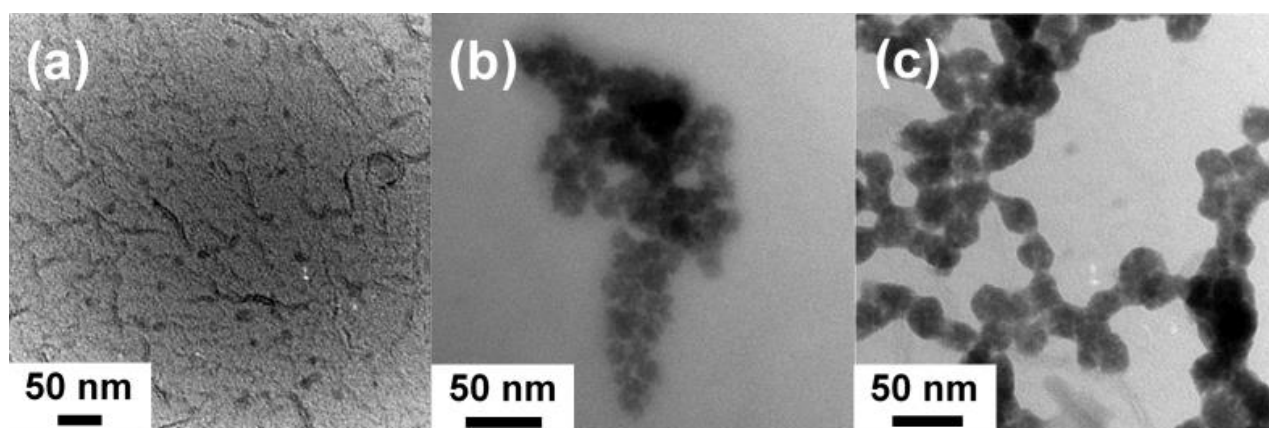


Figure 4: Nanoparticles obtained after 30 s reaction time: (a) small, individual nanoparticles, (b) raspberry-like, larger nanoparticles, intermediate state, and (c) raspberry-like, larger nanoparticles, final state.

Atomic force microscopy (AFM) as an additional method of size determination was applied to confirm the TEM results of the sample obtained after 30 s reaction time. AFM enables imaging of the nanoparticles under milder conditions than TEM and ambient conditions so that thermal damage of the nanostructures due to the electron beam can be excluded [32]. The data of the AFM measurements are displayed in Fig. 4.

On the one hand, one can see single deflection peaks in Fig. 5 (a), which are 1.5 and 2.3 nm in width (green and red marks). On the other hand, Fig. 5 (b) shows four deflection peaks directly next to each other. The peaks' width is about 3.5 nm (red mark), and they appear rather individually. It is suggested that these single deflection peaks correspond to the type 0 nanoparticles already found in TEM (Fig. 4 (a)). The size difference to the TEM data is likely due to damage by the electron beam, which causes the particles to appear larger. Consequently, the stacked deflection peaks (Fig. 5 (b), 14.7 nm, red + green mark) correspond to a nanoparticle cluster similar to those found in Fig. 4 (b).

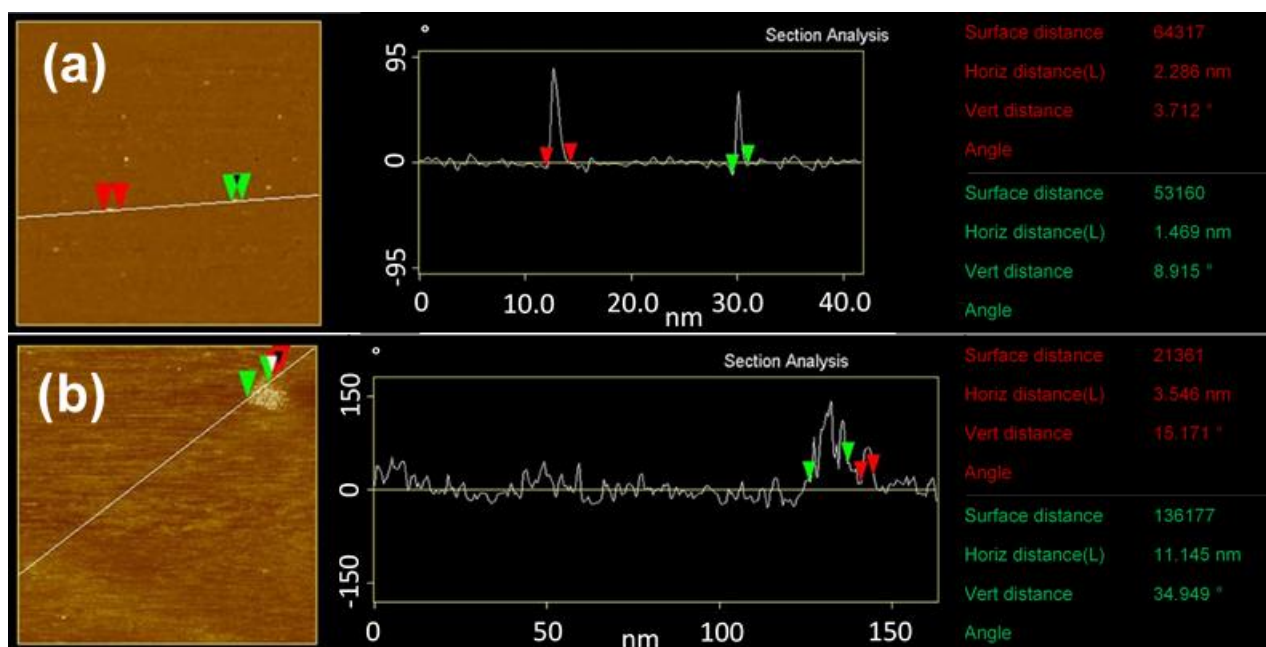


Figure 5: AFM measurements of nanoparticles obtained after 30 s reaction time: (a) individual single nanoparticles and (b) cluster of small nanoparticles of about the same size as the individual ones in (a). Both images are taken from the same sample. The results contain the measured area with height differences displayed in different brightness, a height evaluation along a drawn line (lever deflection in ° vs. distance in nm), and a sum-up of marked distances along the drawn line. The particle/cluster size is given as the horizontal distance (Horiz distances(L)).

Chemical composition

To confirm the XRD results for stibnite and to examine the amorphous particles' composition, an energy dispersive x-ray (EDX) analysis was performed in conjunction with SEM for selected samples obtained after reaction times from 2 min to 30h. It was not possible to examine the samples obtained after 30 s since the yield is too low at this reaction stage. The sample, which reacted for 2 min (Fig. 6 (a)), contained less sulfur than expected by the stoichiometric ratio of Sb_2S_3 . However, the results of the samples obtained after reaction times between 5 min and 30 h are all in good agreement with the stoichiometric ratio of antimony and sulfur in Sb_2S_3 (Tab. 1, Fig. 6 (b), and Fig. S6 in the Supplementary Information).

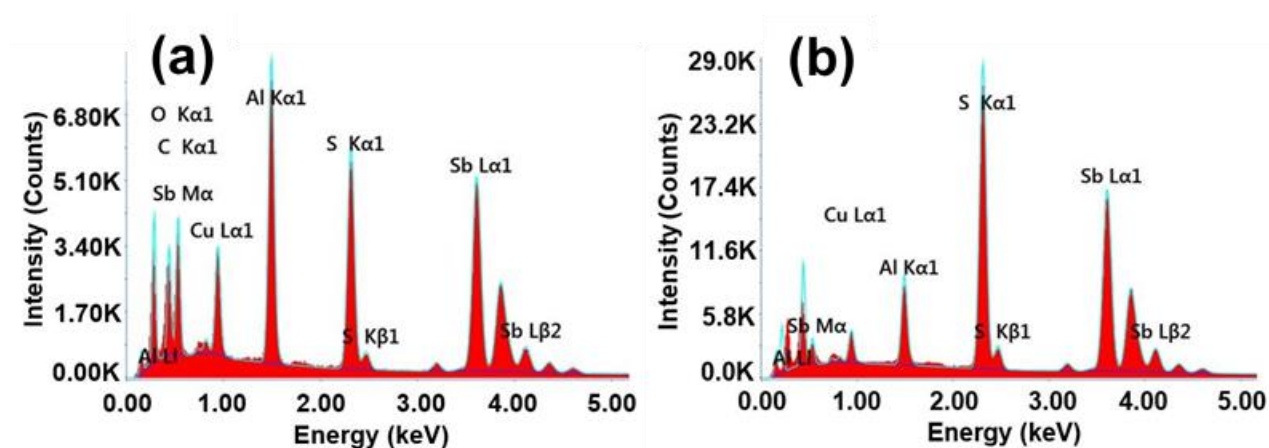


Figure 6: EDX spectra of the nanoparticles obtained after (a) 2 min and (b) 5 min reaction duration. The samples were measured on a carbon-coated copper grid on an aluminum holder, explaining the detection of these elements. Oxygen may have been detected due to contamination of the sample, the grid or the holder.

The non-stoichiometric Sb:S ratio in the early reaction stage is probably due to the oleylamine used in the synthesis. Several authors have already described that hydrolysis of antimony in fatty amines can lead to the formation of Sb_2O_3 [33–35]. Baum et al. obtained cubic $\alpha\text{-Sb}_2\text{O}_3$ (senarmontite) when they performed a synthesis

to obtain copper thioantimonate, by injecting a heated (60°C) and degassed S-OIAM precursor into a heated (200-250°C) and degassed mixture of Cu(I)Cl, Sb(III)Cl₃, and OIAM, but omitted both sulfur and Cu(I)Cl [33]. In contrast, they could synthesize the desired copper thioantimonate when they used Sb₂O₃ instead of Sb(III)Cl₃ in a following synthesis. They concluded that Sb₂S₃ works as an intermediate product rather than as a byproduct.

To show that antimony oxide can also be formed under the reaction conditions used in this work, the Sb precursor was injected directly into the oleylamine at 150°C without adding sulfur, and the solution turned white immediately. Fig. 7 shows the SEM and XRD results of the white product obtained by this reaction. The yielded nanoparticles are 60±15 nm in diameter and can be assigned to the cubic α-phase of Sb₂O₃, senarmontite (COD 1011201).

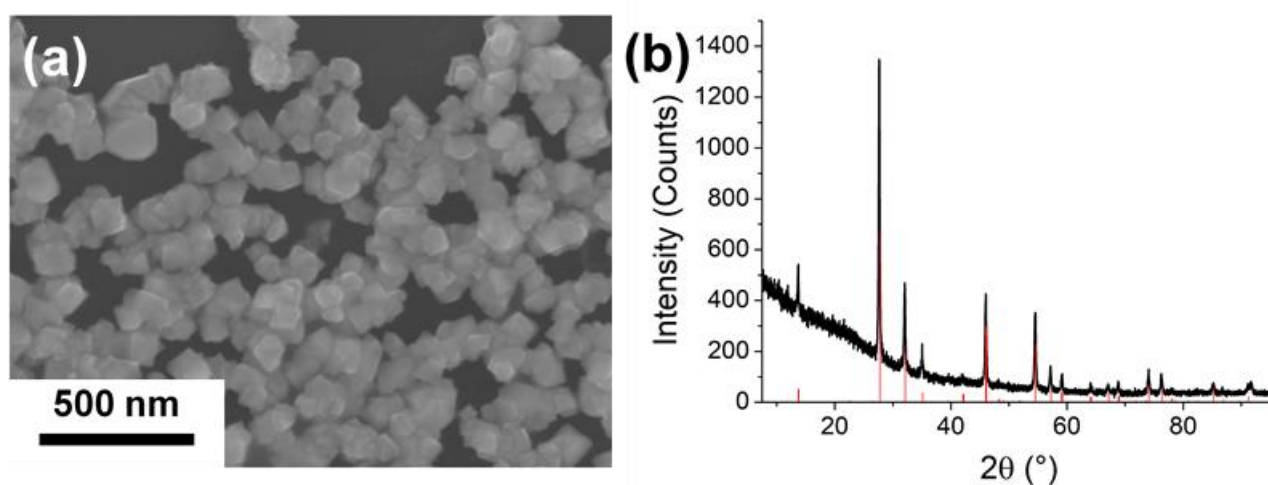


Figure 7: Measurement results of the white product obtained by the direct injection of the Sb precursor into oleylamine at 150°C without the addition of sulfur: (a) SEM image and (b) XRD pattern (Red lines are corresponding to the diffraction peaks of senarmontite, COD 1011201).

These results indicate that the first species formed consist of a compound of antimony, sulfur, and oxygen, with the oxygen being replaced by sulfur with increasing reaction

time while the nanoparticles transform into pure Sb_2S_3 . This species could act as an intermediate for the particles formed at later stages or as an intermediate species formed parallel to the main reaction. It is also possible that initially, a species forms, which contains antimony, sulfur and carbon-residues from the precursors, as it has been found in high-temperature seeding processes from other metallo-organic syntheses [36]. A changing chemical composition could also be a reason for the nanoparticles to undergo a second hierarchical assembly. A similar behavior was found by Liu et al., who synthesized cobalt particles with a cobalt alkoxide intermediate [25].

Fig. 8 summarizes the results discussed above and suggests a growth mechanism for Sb_2S_3 : Instantly after injecting the colorless Sb-EHA precursor into the clear yellowish S-OIAm precursor solution at 150°C , the reaction mixture turns orange before it turns red about 30 s later but stayed clear. At this stage, type 0 seed particles of a size of 2-4 nm (diameter determined by AFM) are formed, which assemble into 20-40 nm large clusters. These particles are amorphous and do not have a stoichiometric ratio corresponding to Sb_2S_3 . When 2 min have passed, the mixture becomes turbid and changes back to an orange color. The clustered type 0 seeds merged into type I nanoparticles of about 35 nm in diameter, which begin to aggregate again into spherical structures of about 200 nm in size. At this point, the particles' chemical composition complies with Sb_2S_3 . The color becomes darker and starts turning red (~20 min) since the aggregates merge into type II particles which seem to assemble into the superordinated type III structures. After 7-9 h, the solution becomes brownish. Most likely, this is the point at which significant crystallization begins as some of the amorphous type III structures act as crystallization nuclei. The orthorhombic crystals

grow, probably at the expense of the amorphous particles, until a grayish-black mixture of crystalline material without spherical, amorphous particles (~18 h) is finally obtained.

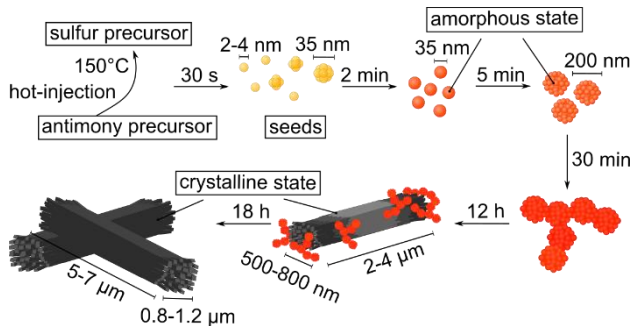


Figure 8: Growth scheme of Sb_2S_3 . After injection, type 0 seeds (yellow) are formed, which turn into small type I amorphous nanoparticles (orange). These small particles aggregate and merge into type II nanoparticles (red), which assemble into superordinated type III structures before crystallizing. The crystals (black) grow at the expense of the amorphous nanoparticles in an Ostwald ripening process.

Optical characterization

The materials' optical properties were measured by reflectance spectroscopy and analyzed by applying the Tauc plot to receive the band gap values of the material [37, 38]. As shown in Eq. 1, the absorption coefficient α is expressed by the Planck constant h , the photon's frequency ν , a constant B , which Davis and Mott described as the magnitude of the optical absorption constant [38], and a transition factor γ :

$$(\alpha h\nu)^{1/\gamma} = B(h\nu - E_g) \quad (1)$$

The transition factor γ depends on the type of the band gap transition. It equals 1/2 for a direct allowed transition and 2 for an indirect allowed transition.

For reflectance data, α is expressed by the Kubelka-Munk function $F(R_\infty)$ (Eq. 2), which is the quotient of the absorption coefficient k and the scattering coefficient s , which, in turn, is correlated to the reflectance of an infinitely thick specimen R_∞ [39]:

$$F(R_\infty) = \frac{k}{s} = \frac{(1 - R_\infty)^2}{2R_\infty} \quad (2)$$

In the literature, there are different opinions regarding the type of electron transition of Sb_2S_3 . Some authors assume a direct transition for the amorphous and the crystalline material [30, 40, 41], while others propose an indirect transition [42–45].

However, amorphous materials exhibit neither an indirect nor a direct transition as these materials are highly disordered and do not have a band structure based on the Bloch theorem. Nevertheless, the electronic states in amorphous materials can be divided into localized and delocalized states, forming a so-called mobility gap [46]. Initially, the Tauc plot (Eq. 1) was used to calculate band gap values for amorphous materials, i.e., mobility gaps, with a transition factor γ equal to 2 [37]. Hence, an amorphous material can mathematically be treated as a material with an indirect allowed transition.

For crystalline Sb_2S_3 , Filip et al. [47] and Vadapoo et al. [48] did first-principle calculations of the band structures. Both found indirect transitions as energetically most favorable but with only a little difference to a direct transition. They concluded that the direct transition would most likely be dominant, especially at ambient temperature. Filip et al. defined the band gap as "effectively direct gap". Therefore, and because most references assume a direct transition, the transition will be considered

a direct one in the present work. In contrast, Validžić et al. performed calculations based on the density functional theory and found a direct band gap [31].

The measured reflectance data can be seen in Fig. 9 (a). They show that the onsets of the spectra of the different samples shift towards higher wavelengths with increasing reaction time. The spectrum obtained after 12 h reaction time exhibits two slopes at $\lambda < 670$ nm and $\lambda > 670$ nm, likely due to amorphous and crystalline particles' simultaneous presence. Although SEM images indicate (see Fig. 1 (e)) that the sample obtained after 16 h still contains some amorphous particles, their influence on the optical behavior seems negligible since the second slope is no more visible.

Fig. 9 (b) and (c) show the Tauc plots of the amorphous and crystalline samples. The two slopes of the sample obtained after 12 h reaction time were fitted individually as indirect and direct transition, assuming that the first slope ($\lambda < 670$ nm) corresponds to the amorphous and the second slope ($\lambda > 670$ nm) to the crystalline particles. As one can see, the band gap values change throughout the different samples (values in Tab. 1) and depend on the reaction time and crystallinity of the sample. While the particles after 2 min reaction time have a band gap value of 2.18 eV, this value decreases to 2.01 eV after 12 h.

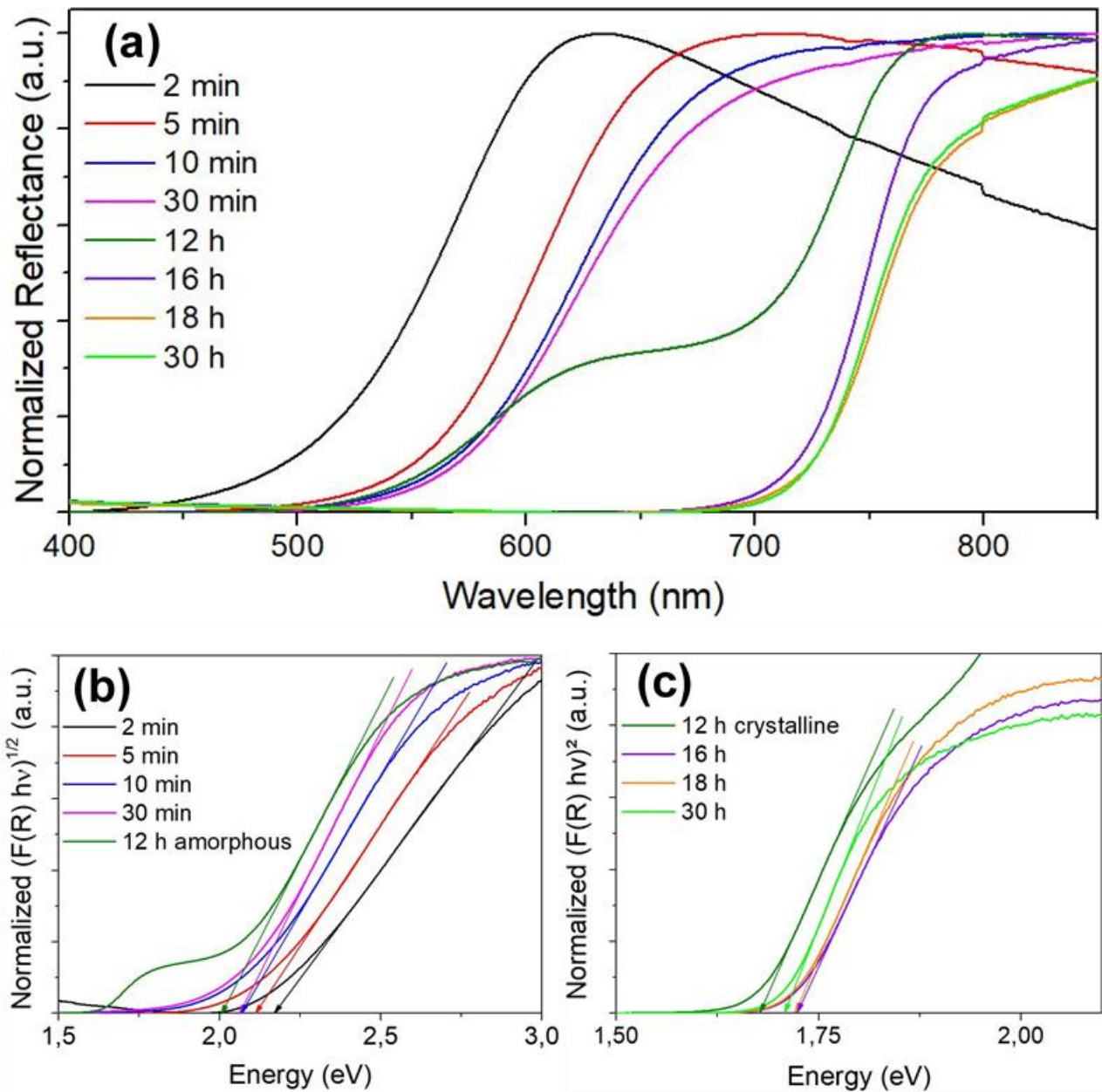


Figure 9: Optical characterization of Sb_2S_3 samples obtained after different reaction times: (a) reflectance spectra, (b) Tauc plots of the spectra of the amorphous particles, and (c) Tauc plots of the spectra of the crystalline particles. All spectra were normalized to the maximum intensity. The band transitions of the amorphous particles are treated as allowed, indirect transitions, while the transitions of the crystalline material are considered to be allowed, direct transitions. Tangents were drawn at the slope of each graph to estimate the band gap value. The sample obtained after 12 h reaction time exhibits two slopes which correspond to the absorption of amorphous ($\lambda < 670$ nm) and crystalline ($\lambda > 670$ nm) particles present.

There are already different band gap values reported for amorphous Sb_2S_3 nanomaterials. For example, Abulikemu et al. reported a value of 2.15 eV while Wang et al. reported 2.02 eV for nanoparticles received from a hot-injection synthesis using different solvents [19, 17]. Variation in band gap values is also known to occur in other amorphous semiconductors, e.g., amorphous, hydrogenated silicon. This is explained by different preparation conditions [49]. Different formation mechanisms can lead to different bonding lengths and angles in an amorphous material and, therefore, to a different mobility gap [46]. Hence, a decreasing mobility gap suggests that an electronic relaxation process occurs after longer reaction times. The band fluctuations and the bonding lengths and angles get closer to the band and material structure of the corresponding crystalline modification until crystallization itself starts.

The material shows a different band gap energy after the crystallization has started. All samples containing crystalline particles have a band gap energy of around 1.70 eV, independent of the reaction time. This value agrees well with previously reported values for crystalline Sb_2S_3 particles of a similar size [50].

Conclusion

The formation mechanism of Sb_2S_3 nanoparticles via a hot-injection synthesis at 150°C is revealed. In this way, we could gain a more in-depth insight into the kinetics of particle formation, while earlier studies of Abulikemu et al. and Li et al. were focusing on the temperature-dependent evolution of Sb_2S_3 particles. The suggested mechanism assumes that seeds (type 0 particles) are formed directly after injecting the antimony precursor into the sulfur precursor. These seeds merge into type I amorphous nanoparticles containing a smaller percentage of sulfur than the expected

stoichiometric ratio of Sb and S, possibly due to oxygen being involved in the seeding process. Subsequently, the type I nanoparticles aggregate into type II nanoparticles and form superordinated type III structures that finally crystallize in an orthorhombic crystal structure.

Furthermore, the kinetic control of the reaction enables tuning of the optical band gap of the amorphous material in the range of 2.18 ± 0.03 to 2.01 ± 0.03 eV. In contrast, the optical band gap of the crystalline particles decreased to a value of 1.71 ± 0.03 eV and did not change any further. The reduction of the mobility gap of the amorphous states of the particles is likely due to an electronic relaxation effect with increasing reaction time.

With the knowledge provided by this study, different strategies can be developed capable of controlling the size of the amorphous and crystalline particles on an even broader range than it has been done up to now. In this way, the customizable application of Sb_2S_3 nanomaterial in solar cells and other fields of electronics and optoelectronics will be enhanced.

Experimental

All experiments were carried out using standard glass equipment. The reaction vessels were cleaned before use with nitric acid (65 vol. %, VWR Chemicals) and were subsequently repeatedly rinsed with deionized (DI) water. The nanoparticles were redispersed using an ultrasonic bath (Sonorex RK512H (860 W, 35 kHz) from Bandelin). A controlled heating rate and temperature in the reaction vessel was achieved by a temperature controller (LTR 3500, Juchheim Solingen). Injections into the reaction vessel were performed with a 14 gauge cannula (L = 200 mm, neoLab).

Materials

Antimony(III) chloride (Sb(III)Cl_3 , >99.95 %), sulfur (S, 99.98 %), 2-ethylhexanoic acid (EHA, >99 %), paraffin oil (visc. liq., $d = 0.827\text{-}0.890$ g/mL), oleylamine (OIAM, 70 %) and isopropyl alcohol (IPA, 99.5 %) were obtained by Sigma-Aldrich. Hexane (>98 %) was purchased by Alfa Aesar, chlorobenzene (>99 %) by Merck KGaA, and 1,2-dichlorobenzene (>98 %) by Fisher Scientific. All chemicals were used without further purification.

Synthesis

Undoped Sb_2S_3 nanoparticles

All reaction steps were performed under an argon atmosphere.

Prior to the reaction, two precursor solutions were freshly prepared. First, the sulfur precursor, an S-OIAM solution, was produced by dissolving 1.5 mmol elemental sulfur in 6 mL OIAM via sonification in an ultrasonic bath for 10 min. Afterward, 25 mL paraffin oil was added. The solution was heated to 150°C with a heating rate of 3.3 K/min under magnetic stirring (800 rpm). Second, an Sb(III) complex solution was prepared by adding 1 mmol Sb(III)Cl_3 to 5 mL EHA. The mixture was magnetically stirred (750 rpm) and heated up to 90°C in an oil bath.

When both precursor solutions reached the desired temperatures, the Sb precursor was swiftly injected into the S precursor solution, and the reaction mixture was kept under magnetic stirring (800 rpm) at 150°C for 60 s to 30 h.

To stop the reaction, the heating mantle under the reaction vessel was replaced by an ice bath, and 15 mL hexane was injected into the reaction. The received product was

precipitated by adding 30 mL IPA and separated by centrifugation at 50-2500 g for 5-20 min (depending on the reaction time; for details, s. Tab. S1 in the Supporting Information). The precipitate was redispersed in 20 mL of a 2:3 mixture (volumetric) of chlorobenzene and 1,2-dichlorobenzene (HAS) [22]. Precipitation and centrifugation were repeated twice. For the second redispersion step, 20 mL hexane instead of HAS was used. Finally, the nanoparticles were redispersed in 20 mL IPA.

Characterization

Scanning electron microscopy (SEM)

SEM images were recorded with a Hitachi SU 5000 scanning electron microscope in SE mode with an electron acceleration voltage of 15 kV and a spot intensity of 40. The working distance was 3 mm. A droplet of a dispersion ($c = 1.5\text{-}2\text{ g/L}$) of the particles in IPA was dried on a carbon-coated copper grid (carbon-coating type A, 6-10 nm thickness, Cu 200 mesh, Plano GmbH). The software FIJI was used to evaluate the particle size for 200-300 particles per synthesis on several images [51].

Transmission electron microscopy (TEM)

A Zeiss EM 109 was used at 80 kV acceleration voltage to record the TEM images. The grid preparation and image processing were performed as stated above for SEM.

Atomic force microscopy (AFM)

Atomic force microscopy (AFM) was performed with a Multimode quadrex SPM with Nanoscope IIIe controller (Veeco Instrument Inc) operated under ambient conditions to determine the particle size using the sample in the form of a highly diluted solution.

The drive frequency was kept constant during the imaging, while the drive amplitude was set to 7171 mV.

Energy-dispersive X-ray analysis (EDX)

Elemental analysis was performed with an EDAX X-ray detector (Octane Elect Plus) attached to the SEM. The SEM was run with an acceleration voltage of 15 kV and a spot intensity of 50. The working distance was 10 mm. The resolution of the detector was 126.2 eV.

Reflectance measurements

Reflectance measurements were performed with a Cary 5000 UV-Vis-NIR spectrometer (Agilent Technologies) equipped with an integrating sphere (internal DRA 2500). Particles were measured as a dispersion in IPA ($c = 2\text{--}2.5$ g/L) in standard cuvettes made of special optical glass (OS, Hellma) in the range of 400 to 850 nm.

At 800 nm, the instrument's detector changes, which causes a small artifact at this wavelength. While this artifact is visible in Fig. 7 (a), it gets negligible in Fig. 7 (b) and (c) because it corresponds to an energy of 1.55 eV, which is not in a relevant range for the band gap analysis of the measured samples, and the intensity decreases to a non-visible level. The estimation of the accuracy of the Tauc method was based on a study by Viezbicke et al., who evaluated the accuracy of the Tauc plot for 120 individual analyses of polycrystalline ZnO and found a deviation of about 0.03 eV [52].

X-ray diffraction spectrometry (XRD)

For XRD measurements, a minimum amount of 10 mg of dried particles was used. The samples were measured in a capillary in transmission geometry.

Two different diffractometers were used to perform the measurements. The first XRD device was a Bruker D8 Advanced equipped with a LYNXEYE XE-T detector and a Cu $K_{\alpha 1}$ radiation source (40 kV, 40 mA) with a radiation wavelength of 0.15405 nm. The angle range of the measurements was 6-80° 2θ with a step size of 0.025°. The second device was a STOE STADI P equipped with a Dectris MYTHEN2 R detector and a Cu $K_{\alpha 1}$ radiation source (40 kV, 40 mA) with a radiation wavelength of 0.15405 nm. The angle range of the measurements was 6-96° 2θ with a step size of 0.015°.

Supporting Information

Supporting Information:

File Name: Sb2S3_NP_Supporting Information.pdf

File Format: PDF

Title: Additional SEM and TEM images, EDX data, and synthesis details

Acknowledgments

We thank Dr. Michael Evans from Bruker Corporation and Michael Teck from STOE & Cie GmbH for recording the X-ray diffractograms.

Financial Support

The research was funded by the Bilateral project between the Federal Republic of Germany and the Republic of Serbia, funded by the Serbian Ministry of Education, Science and Technological Development (grant 451-03-01971/2018-09/19) and the German Academic Exchange Service (DAAD) within the PPP Serbia program (grant 57447826). This work was supported by a fellowship of the Platform for Ph. D. students

of the Technical University of Darmstadt and the Darmstadt University of Applied Sciences.

References

1. Smil, V.; *OECD Observer* **2006**, 19, 22–24.
2. Versavel, M. Y.; Haber, J. A. *Thin Solid Films* **2007**, 515, 7171–7176.
doi:10.1016/j.tsf.2007.03.043
3. Tang, R.; Wang, X.; Jiang, C.; Li, S.; Jiang, G.; Yang, S.; Zhu, C.; Chen, T. *J. Mater. Chem. A* **2018**, 6, 16322–16327. doi:10.1039/C8TA05614E
4. Validžić, I. L.; Janošević, V.; Mitrić, M. *Environ. Prog. Sustainable Energy* **2016**, 35, 512–516. doi:10.1002/ep.12221
5. Cao, F.; Liu, W.; Zhou, L.; Deng, R.; Song, S.; Wang, S.; Su, S.; Zhang, H. *Solid State Sciences* **2011**, 13, 1226–1231.
doi:10.1016/j.solidstatesciences.2011.02.007
6. Shaji, S.; Arato, A.; O'Brien, J. J.; Liu, J.; Castillo, G. A.; Palma, M. I. M.; Roy, T. K. D.; Krishnan, B. *J. Phys. D: Appl. Phys.* **2010**, 43, 75404. doi:10.1088/0022-3727/43/7/075404
7. Itzhaik, Y.; Niitsoo, O.; Page, M.; Hodes, G. *J. Phys. Chem. C* **2009**, 113, 4254–4256. doi:10.1021/jp900302b
8. Zakaznova-Herzog, V. P.; Harmer, S. L.; Nesbitt, H. W.; Bancroft, G. M.; Flemming, R.; Pratt, A. R. *Surf. Sci.* **2006**, 600, 348–356.
doi:10.1016/j.susc.2005.10.034
9. Lou, W.; Chen, M.; Wang, X.; Liu, W. *Chem. Mater.* **2007**, 19, 872–878.
doi:10.1021/cm062549o

10. Ota, J.; Roy, P.; Srivastava, S. K.; Nayak, B. B.; Saxena, A. K. *Cryst. Growth Des.* **2008**, *8*, 2019–2023. doi:10.1021/cg701133b
11. Salinas-Estevané, P.; Sánchez, E. M. *Cryst. Growth Des.* **2010**, *10*, 3917–3924. doi:10.1021/cg100365z
12. Salem, A. M.; Selim, M. S. *J. Phys. D: Appl. Phys.* **2001**, *34*, 12–17. doi:10.1088/0022-3727/34/1/303
13. Murtaza, G.; Akhtar, M.; Azad Malik, M.; O'Brien, P.; Revaprasadu, N. *Mater. Sci. Semicond. Process.* **2015**, *40*, 643–649. doi:10.1016/j.mssp.2015.07.038
14. Talapin, D. V.; Lee, J.-S.; Kovalenko, M. V.; Shevchenko, E. V. *Chem. Rev.* **2010**, *110*, 389–458. doi:10.1021/cr900137k
15. Yao, X.; Zhang, Y.; Du, L.; Liu, J.; Yao, J. *Renewable Sustainable Energy Rev.* **2015**, *47*, 519–539. doi:10.1016/j.rser.2015.03.078
16. Kwon, S. G.; Hyeon, T. *Small* **2011**, *7*, 2685–2702. doi:10.1002/smll.201002022
17. Wang, W.; Strössner, F.; Zimmermann, E.; Schmidt-Mende, L. *Sol. Energy Mater. Sol. Cells* **2017**, *172*, 335–340. doi:10.1016/j.solmat.2017.07.046
18. Deng, Z.; Mansuripur, M.; Muscat, A. J. *Nano Lett.* **2009**, *9*, 2015–2020. doi:10.1021/nl9002816
19. Abulikemu, M.; Del Gobbo, S.; Anjum, D. H.; Malik, M. A.; Bakr, O. M. *J. Mater. Chem. A* **2016**, *4*, 6809–6814. doi:10.1039/c5ta09546h
20. Validžić, I. L.; Abazović, N. D.; Mitrić, M. *Met. Mater. Int.* **2012**, *18*, 989–995. doi:10.1007/s12540-012-6010-7
21. Li, L.; Yang, L.; Fu, B.; Li, Z. *Bull Mater Sci* **2020**, *43*. doi:10.1007/s12034-020-02121-7
22. Wang, R.; Shen, B.; Sun, H.; Zhao, J. *J. Chem. Eng. Data* **2018**, *63*, 553–558. doi:10.1021/acs.jced.7b00699

23. Roca, R. A.; Leite, E. R. *J. Am. Ceram. Soc.* **2013**, *96*, 96–102.
doi:10.1111/jace.12078
24. Bamiduro, F.; Ward, M. B.; Brydson, R.; Milne, S. J. *J. Am. Ceram. Soc.* **2014**, *97*, 1619–1624. doi:10.1111/jace.12809
25. Liu, Q.; Guo, X.; Li, Y.; Shen, W. *J. Phys. Chem. C* **2009**, *113*, 3436–3441.
doi:10.1021/jp8081744
26. Geng, Z. R.; Wang, M. X.; Yue, G. H.; Yan, P. X. *J. Cryst. Growth* **2008**, *310*, 341–344. doi:10.1016/j.jcrysgr.2007.10.052
27. Zhang, L.; Chen, L.; Wan, H.; Zhoul, H.; Chen, J. *Cryst. Res. Technol.* **2010**, *45*, 178–182. doi:10.1002/crat.200900535
28. Wang, H.; Lu, Y.-N.; Zhu, J.-J.; Chen, H.-Y. *Inorg. Chem.* **2003**, *42*, 6404–6411.
doi:10.1021/ic0342604
29. Tao, W.; Wang, J.; Wu, D.; Chang, J.; Wang, F.; Gao, Z.; Xu, F.; Jiang, K. *Dalton Trans.* **2013**, *42*, 11411–11417. doi:10.1039/c3dt51439k
30. Wang, G.; Cheung, C. L. *Mater. Lett.* **2012**, *67*, 222–225.
doi:10.1016/j.matlet.2011.09.074
31. Validžić, I. L.; Mitrić, M.; Abazović, N. D.; Jokić, B. M.; Milošević, A. S.; Popović, Z. S.; Vukajlović, F. R. *Semicond. Sci. Technol.* **2014**, *29*, 35007.
doi:10.1088/0268-1242/29/3/035007
32. Grobelny, J.; DelRio, F. W.; Pradeep, N.; Kim, D.-I.; Hackley, V. A.; Cook, R. F. *Methods Mol. Biol.* **2011**, *697*, 71–82. doi:10.1007/978-1-60327-198-1_7
33. Baum, F.; Pretto, T.; Brolo, A. G.; Santos, M. J. L. *Cryst. Growth Des.* **2018**, *18*, 6521–6527. doi:10.1021/acs.cgd.8b00667
34. Christian, P.; O'Brien, P. *J. Mater. Chem.* **2005**, *15*, 4949. doi:10.1039/b511952a
35. Zou, Y.; Jiang, J. *Mater. Lett.* **2014**, *123*, 66–69. doi:10.1016/j.matlet.2014.02.069

36. Bronstein, L. M.; Huang, X.; Retrum, J.; Schmucker, A.; Pink, M.; Stein, B. D.; Dragnea, B. *Chem. Mater.* **2007**, *19*, 3624–3632. doi:10.1021/cm062948j
37. Tauc, J.; Grigorovici, R.; Vancu, A. *Phys. Stat. Sol. (b)* **1966**, *15*, 627–637. doi:10.1002/pssb.19660150224
38. Davis, E. A.; Mott, N. F. *Philos. Mag.* **1970**, *22*, 903–922. doi:10.1080/14786437008221061
39. Kubelka, P.; Munk, F. *Z. Tech. Phys.* **1931**, 593–601.
40. Han, Q.; Sun, S.; Sun, D.; Zhu, J.; Wang, X. *RSC Adv.* **2011**,, 1364. doi:10.1039/c1ra00379h
41. Lei, H.; Lin, T.; Wang, X.; Zhang, S.; Cheng, Q.; Chen, X.; Tan, Z.; Chen, J. *Mater. Lett.* **2018**, *233*, 90–93. doi:10.1016/j.matlet.2018.08.058
42. Gao, C.; Huang, J.; Li, H.; Sun, K.; Lai, Y.; Jia, M.; Jiang, L.; Liu, F. *Ceram. Int.* **2019**, *45*, 3044–3051. doi:10.1016/j.ceramint.2018.10.155
43. Yesugade, N. S.; Lokhande, C. D.; Bhosale, C. H. *Thin Solid Films* **1995**, *263*, 145–149. doi:10.1016/0040-6090(95)06577-6
44. Țigașu, N.; Gheorghieș, C.; Rusu, G. I.; Condurache-Bota, S. *J. Non-Cryst. Solids* **2005**, *351*, 987–992. doi:10.1016/j.jnoncrysol.2004.12.014
45. Perales, F.; Lifante, G.; Agulló-Rueda, F.; Heras, C. d. I. *J. Phys. D: Appl. Phys.* **2007**, *40*, 2440–2444. doi:10.1088/0022-3727/40/8/005
46. Kasap, S.; Capper, P. *Springer Handbook of Electronic and Photonic Materials*; Springer International Publishing: Cham, 2017.
47. Filip, M. R.; Patrick, C. E.; Giustino, F. *Phys. Rev. B* **2013**, *87*. doi:10.1103/PhysRevB.87.205125
48. Vadapoo, R.; Krishnan, S.; Yilmaz, H.; Marin, C. *Nanotechnology* **2011**, *22*, 175705. doi:10.1088/0957-4484/22/17/175705

49. Pyskin, S. L.; Ballato, J. *Long-Term Convergence of Bulk- and Nano-Crystal Properties*; INTECH Open Access Publisher, **2011**. doi: 10.5772/21418
50. Chao, J.; Liang, B.; Hou, X.; Liu, Z.; Xie, Z.; Liu, B.; Song, W.; Chen, G.; Di Chen; Shen, G. *Opt. Express* **2013**, *21*, 13639–13647.
doi:10.1364/OE.21.013639
51. Schindelin, J.; Arganda-Carreras, I.; Frise, E.; Kaynig, V.; Longair, M.; Pietzsch, T.; Preibisch, S.; Rueden, C.; Saalfeld, S.; Schmid, B.; Tinevez, J.-Y.; White, D. J.; Hartenstein, V.; Eliceiri, K.; Tomancak, P.; Cardona, A. *Nat. Methods* **2012**, *9*, 676–682. doi:10.1038/nmeth.2019
52. B. D. Vezbicke, S. Patel, B. E. Davis, D. P. Birnie, *Phys. Status Solidi B* **2015**, *252*, 1700-1710. doi: 10.1002/pssb.201552007